Variability of the Reconnection Guide Field in Solar Flares

Joel T Dahlin[1], Spiro K Antiochos[1], Jiong Qiu[2], and C Richard Devore[1]

[1]NASA Goddard Space Flight Center
[2]Montana State University

November 25, 2022

Abstract

Solar flares may be the best-known examples of the explosive conversion of magnetic energy into bulk motion, plasma heating, and particle acceleration via magnetic reconnection. The energy source for all flares is the highly sheared magnetic field of a filament channel above a polarity inversion line (PIL). During the flare, this shear field becomes the so-called reconnection guide field (i.e., the non-reconnecting component), which has been shown to play a major role in determining key properties of the reconnection including the efficiency of particle acceleration. We present new high-resolution, three-dimensional, magnetohydrodynamics simulations that reveal the detailed evolution of the magnetic shear/guide field throughout an eruptive flare. The magnetic shear evolves in three distinct phases: shear first builds up in a narrow region about the PIL, then expands outward to form a thin vertical current sheet, and finally is transferred by flare reconnection into an arcade of sheared flare loops and an erupting flux rope. We demonstrate how the guide field may be inferred from observations of the sheared flare loops. Our results indicate that initially the guide field is larger by about a factor of 5 than the reconnecting component, but it weakens by more than an order of magnitude over the course of the flare. Instantaneously, the guide field also varies spatially over a similar range along the three-dimensional current sheet. We discuss the implications of our results for understanding observations of flare particle acceleration.

Posted on 25 Nov 2022 — CC-BY-NC-ND 4 — https://doi.org/10.1002/essoar.10508183.1 — This a preprint and has not been peer reviewed. Data may be preliminary.

Draft version October 7, 2021
Typeset using LaTeX **preprint** style in AASTeX63

Variability of the Reconnection Guide Field in Solar Flares

Joel T. Dahlin,[1] Spiro K. Antiochos,[1] Jiong Qiu,[2] and C. Richard DeVore[1]

[1] *Heliophysics Science Division, NASA Goddard Space Flight Center, Greenbelt, MD 20771*
[2] *Department of Physics, Montana State University, Bozeman, MT, 59717*

(Received October 7, 2021; Revised October 7, 2021; Accepted October 7, 2021)

Submitted to ApJ

ABSTRACT

Solar flares may be the best-known examples of the explosive conversion of magnetic energy into bulk motion, plasma heating, and particle acceleration via magnetic reconnection. The energy source for all flares is the highly sheared magnetic field of a filament channel above a polarity inversion line (PIL). During the flare, this shear field becomes the so-called reconnection guide field (i.e., the non-reconnecting component), which has been shown to play a major role in determining key properties of the reconnection including the efficiency of particle acceleration. We present new high-resolution, three-dimensional, magnetohydrodynamics simulations that reveal the detailed evolution of the magnetic shear/guide field throughout an eruptive flare. The magnetic shear evolves in three distinct phases: shear first builds up in a narrow region about the PIL, then expands outward to form a thin vertical current sheet, and finally is transferred by flare reconnection into an arcade of sheared flare loops and an erupting flux rope. We demonstrate how the guide field may be inferred from observations of the sheared flare loops. Our results indicate that initially the guide field is larger by about a factor of 5 than the reconnecting component, but it weakens by more than an order of magnitude over the course of the flare. Instantaneously, the guide field also varies spatially over a similar range along the three-dimensional current sheet. We discuss the implications of our results for understanding observations of flare particle acceleration.

1. INTRODUCTION

The solar atmosphere is replete with explosive activity, from ultraviolet (UV) bursts and Ellerman bombs at the smallest observed scales to spectacular X-class flares and associated coronal mass ejections that drive hazardous space weather. Many of these phenomena are thought to be due to the release of stored magnetic energy by the process of magnetic reconnection. In some remarkable events, much of the energy released is transferred to nonthermal particles, most notably in flares. The most extreme events apparently accelerate all of the coronal electrons (Krucker et al. 2010) and impart the majority of the energy to those energetic particles.

Corresponding author: Joel T. Dahlin
joeltdahlin@gmail.com, joel.t.dahlin@nasa.gov

Such highly efficient electron acceleration is not generally observed in flares, and it is rare or difficult to observe in other instances of coronal reconnection. Two key questions naturally follow. Why is acceleration so efficient in flares? What factors control the considerable flare-to-flare variation of acceleration efficiency? We propose that the *reconnection guide field* of the flare, in particular its evolution during the course of the flare, plays a critical role in the electron acceleration. In this article, we use a numerical model for an eruptive flare to investigate the origin of the guide field in filament channel shear and its subsequent evolution.

It is well known that the highly sheared magnetic field of a filament channel is the energy source for coronal mass ejections and eruptive flares. The coronal magnetic field transitions to a lower-energy state by ejecting this shear in the form of a flux rope. Importantly, during the creation of the flux rope through flare reconnection, the shear participates in the flare energy release as the magnetic field's guide-field component. The guide field is known to play a critical role in controlling the efficiency of plasmoid-associated particle acceleration (Dahlin et al. 2016, 2017; Li et al. 2019; Arnold et al. 2021). Recently, using a hybrid kinetic/magnetohydrodynamic (MHD) model, Arnold et al. (2021) found that reconnection generates power-law nonthermal electron spectra that are highly sensitive to the ratio of the upstream guide field to the reconnecting field. Although the electron heating varied little with guide-field strength, the electron acceleration was suppressed in the regime where the guide field is much stronger than the reconnecting field. Therefore, the guide field appears to determine how efficiently flare-released energy is imparted to nonthermal electrons.

The guide magnetic field in flares is highly challenging to determine directly, due to the difficulty of measuring the coronal magnetic field. Nevertheless, several recent studies have indirectly estimated the guide field in flares. Chen et al. (2020) used Expanded Owens Valley Solar Array (EOVSA; Gary et al. 2013) microwave observations to determine the magnetic-field profile along the current sheet during the 2017 September 10 X-class flare. They found best agreement with an ATHENA flare simulation assuming a guide-field ratio of 0.3. Using an indirect approach, Qiu et al. (2010); Qiu et al. (2017) estimated the guide field in a set of two-ribbon flares. They projected the apparent motion of newly brightened flare-ribbon fronts in the directions parallel and perpendicular to the polarity inversion line (PIL) and estimated the guide-field strength relative to the post-reconnection outflow field. The values ranged from 0.2 to 5.1 with a median value of about 1.

Although indirect measurements of the guide field are sparse, further information can be inferred from the evolution of the flare morphology and energy release. A frequent pattern observed in flares is the so-called "strong-to-weak" shear transition, wherein flare loops (or associated conjugate brightenings in UV or Hα) early in the flare tend to be highly sheared (nearly parallel) to the PIL, but the successively brightening loops are progressively less sheared as the flare evolves (Sakurai et al. 1992; Aschwanden & Alexander 2001; Asai et al. 2003; Su et al. 2006, 2007; Schmahl et al. 2006; Aulanier et al. 2012). This behavior also has been observed in conjugate hard X-ray footpoints (Masuda et al. 2001; Bogachev et al. 2005; Temmer et al. 2007; Ji et al. 2008; Liu et al. 2009; Yang et al. 2009). Sheared structures imply the presence of a guide field at the reconnection site, and the strong-to-weak transition suggests a corresponding weakening of the guide field relative to the reconnecting component. Therefore, one of the objectives of this paper is to draw a quantitative link between the shear and the guide-field strength.

In this article, we investigate the detailed guide-field evolution in new state-of-the-art, high-resolution simulations of an eruptive flare. Critically, we initiate these simulations from a potential-

field configuration in order to model the fully self-consistent evolution of the flare, in particular the buildup of the shear that powers the eruption and becomes the guide magnetic field. In §2, we lay out the role of the shear/guide field in the standard model for eruptive flares. We present our numerical model in §3. The evolution of the shear/guide field during the energy buildup and the eruption is presented in §4. We conclude by discussing the implications of our results for observations in §5.

2. THEORETICAL BACKGROUND

The traditional CSHKP model for eruptive flares (Carmichael 1964; Sturrock 1966; Hirayama 1974; Kopp & Pneuman 1976) interprets the primary morphological features, flare loops and ribbons, according to a reconnection paradigm. Flare loops are formed via reconnection in the corona, and the flare ribbons are illuminated by energy transport from the coronal reconnection sites to the lower levels of the solar atmosphere. This model has been highly successful in interpreting flare observations and has been corroborated by a number of 2.5D MHD simulations (see Shibata & Magara 2011, and references therein). The 2017 September 10 GOES X8.2 flare, in which the vertical current sheet was seen edge-on, strikingly resembled essential features of the CSHKP model including the erupting flux rope (Seaton & Darnel 2018; Long et al. 2018; Veronig et al. 2018; Gopalswamy et al. 2018), trailing current sheet (Seaton & Darnel 2018; Warren et al. 2018; Longcope et al. 2018), and energy deposited by energetic electrons (Gary et al. 2018; Chen et al. 2020).

This standard model has been highly successful in interpreting flare observations, but it neglects several key elements present in actual events. First, the model assumes a simple, laminar current sheet, whereas both observations (Liu et al. 2013; Kumar et al. 2018; Kumar et al. 2019) and theory/modeling (Loureiro et al. 2007; Bhattacharjee et al. 2009; Karpen et al. 2012) have demonstrated that at large Lundquist numbers, reconnection generates numerous turbulent substructures known as plasmoids. Plasmoids are important for both particle acceleration (Drake et al. 2006; Dahlin et al. 2014; Li et al. 2015; Guidoni et al. 2016) and fast energy release (Loureiro et al. 2007; Bhattacharjee et al. 2009; Karpen et al. 2012). The role of plasmoids in flare dynamics and their impact on ribbon structure has recently been examined analytically by Wyper & Pontin (2021). We will discuss these issues further in a forthcoming paper.

Another simplification is that the model essentially considers only the 2D reconnection of antiparallel fields at a magnetic null line ("X line"). In general, three-dimensional reconnection does not require a magnetic null, and there will be a magnetic-field component oriented along the X line and referred to as the guide field (Schindler et al. 1988; Demoulin et al. 1996). There is ample evidence for strong guide fields in the sheared filament channels and flare loops of solar eruptions. The guide field has recently been shown to control both the efficiency of particle acceleration by the Fermi mechanism in plasmoids (Dahlin et al. 2016; Arnold et al. 2021) and the internal structure of the plasmoids themselves. For example, Edmondson & Lynch (2017) found that the correlation length of magnetic fluctuations along the guide-field direction increases with the guide-field ratio.

There have been a number of efforts to extend the CSHKP model to 3D configurations, in particular to establish interpretations for features not captured in the 2D picture, including sigmoids, sheared flare loops, and ribbon morphologies and locations. Using a 3-D numerical model of an eruptive flare triggered by torus instability, Aulanier et al. (2012) found successively reconnected loops diminished in shear, consistent with the observational picture. This was attributed primarily to the spatial distribution of shear in the pre-eruptive field, which was strongest near the PIL, but also to lengthening

of the CME flux-rope field lines prior to flare-reconnection onset that thereby diminished the shear strength.

The evolution of the shear/guide field in an eruptive flare occurs in three phases. It is well-known that CMEs/eruptive flares originate from highly sheared filament channels (Gaizauskas 1998; Gaizauskas et al. 2001; Martin 1998), where the magnetic field is oriented nearly parallel to the polarity inversion line (PIL). The shear-field component is ultimately the energy source for the eruptive flare, and much of the energy release is due to the ejection of the shear field into the heliosphere. The shear contributes excess magnetic pressure that expands the field outward, stressing the system. Regardless of the onset mechanism, in order for significant energy release to occur via the flare reconnection, this energy must be transferred from the shear component to the radial component that is processed by the flare. This occurs primarily by the shear field stretching out the radial field to form a narrow current sheet. When this current sheet reconnects, magnetic flux carrying shear is processed by the flare: the flux ejected upward becomes the toroidal component of the erupting flux rope, and that carried downward becomes the shear in the flare loops. The shear flux, however, is localized to the filament channel, and it is eventually exhausted as the flare reconnection progresses to process unsheared flux outside of the filament channel (e.g. Su et al. 2006). Therefore, the reconnection guide field must weaken substantially over the course of the flare.

We conclude from these arguments that the reconnection guide field is simply the sheared field of the filament channel. An accurate flare model must include the self-consistent response of the coronal magnetic field to the shear buildup and the subsequent creation of the flare current sheet. The details of the magnetic configuration upstream of the current sheet determine where and when the flare begins. In order to investigate the origin and evolution of the guide field, therefore, it is critical to model self-consistently the gradual energy buildup prior to the explosive flare onset.

3. NUMERICAL MODEL

Our eruptive flare simulation was performed with the Adaptively Refined Magnetohydrodynamics Solver (ARMS; DeVore & Antiochos 2008), which has been used to model both CMEs/eruptive flares (see also Lynch et al. 2008, 2009; Karpen et al. 2012; Masson et al. 2013; Lynch et al. 2016; Masson et al. 2019) and the formation of filament channels (Zhao et al. 2015; Knizhnik et al. 2015, 2017a,b, 2018; Dahlin et al. 2019). The magnetic-field configuration (illustrated in Fig. 1a,b) is an idealized active region consisting of two sets of dipoles located just beneath the solar surface at the equator, superposed on a background solar dipole (see Appendix). This combination generates four distinct flux systems in a multipolar "breakout" topology(Antiochos 1998; Antiochos et al. 1999). The antisymmetric magnetic-field profile across the equator generates a null line above the active region that intersects with the solar surface where the PILs cross east and west of the active region. This symmetry is quickly broken by the energy injection as described below. The configuration was chosen so that the flare current sheet would align nearly perfectly with the equator, to simplify the analysis of the shear/guide-field evolution.

The initial atmosphere was a spherically symmetric hydrostatic equilibrium with an inverse-r temperature profile at base temperature $T_s = 2 \times 10^6$ K and pressure $P_s = 4 \times 10^{-1}$ dyn cm^{-2} (as in Dahlin et al. 2019). We solved the ideal MHD equations with an adiabatic temperature equation (as in DeVore & Antiochos 2008; Karpen et al. 2012; Dahlin et al. 2019). The domain extents were $r \in [1R_s, 30R_s]$, $\theta \in [\pi/16, 15\pi/16]$, and $\phi \in [-\pi, +\pi]$. Grid-scale numerical dissipation breaks the frozen-in flux constraint enabling reconnection to occur.

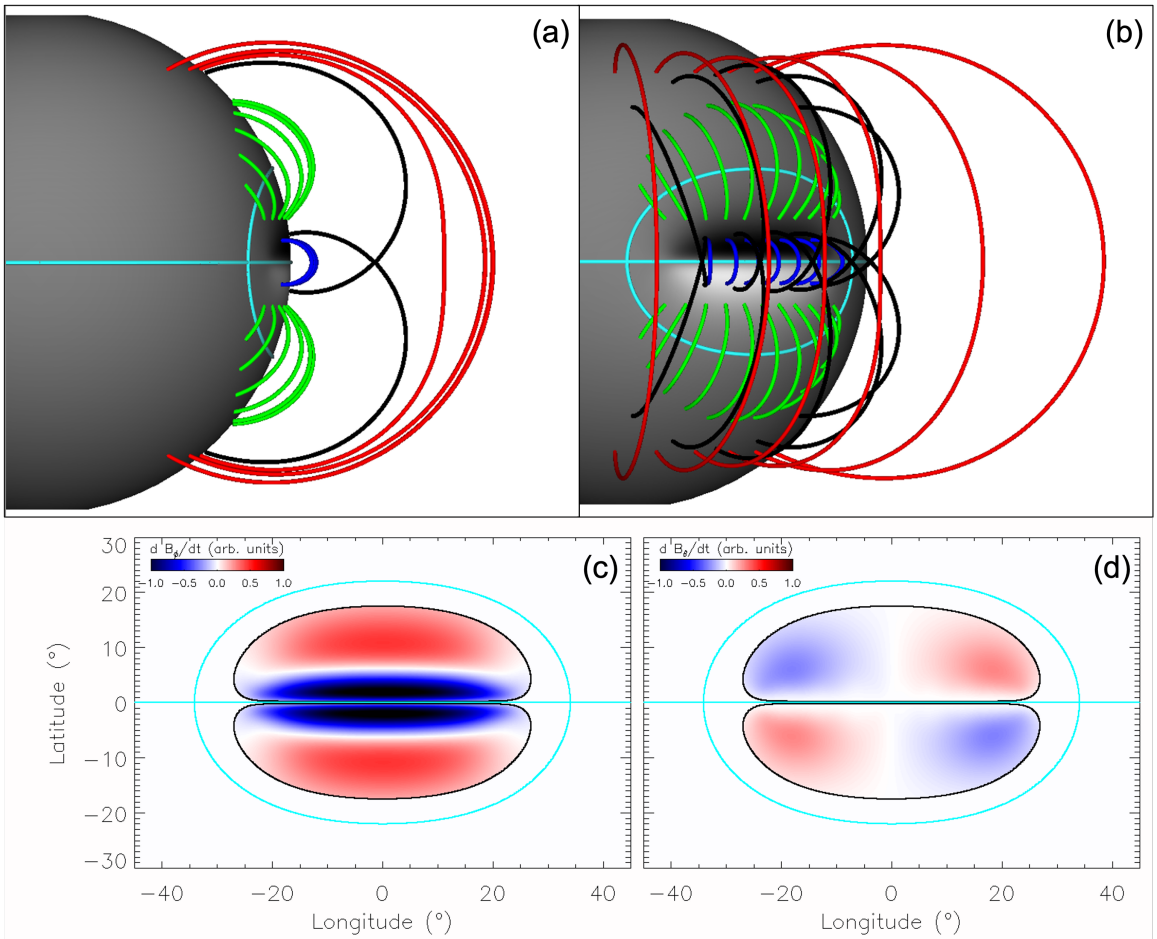

Figure 1. (a,b) Initial magnetic configuration for the eruptive flare simulation. White (black) shading at the inner boundary corresponds to positive (negative) polarity. Polarity inversion lines (PILs) are indicated by cyan curves. Four distinct flux regions are indicated in blue, green, and red (northern and southern sets of green field lines represent distinct flux regions). (c,d) Profile of tangential flux injected by the STITCH method (see text for details) at the inner radial boundary, normalized to 0.58 G s^{-1}.

We used the adaptive-mesh capability of ARMS to resolve selectively important fine-scale structure. The refinement criteria are based on the ratios of the local spatial scale of the electric-current density to the local grid spacing, as in previous high-resolution calculations (Karpen et al. 2012; Masson et al. 2013; Masson et al. 2019). The base (level 1) block structure is $7 \times 7 \times 16$ in r, θ, and ϕ, respectively, and each block contains $8 \times 8 \times 8$ grid cells. For our highest-resolution calculations, a minimum refinement level of 6 is imposed at the innermost boundary over the entire active region ($\theta \in [3\pi/8, 5\pi/8]$, $\phi \in [-\pi/4, \pi/4]$) and a level of 4 over the same angular region for $r \in [1R_s, 2R_s]$. A refinement level of n corresponds to 2^{n-1} times the resolution of the base block structure at level 1. To reduce the computational expense, the overall maximum refinement was held at level 6 during the early energy injection/filament channel stage of the evolution, $t \in [0$ s,11500 s]. Subsequently, the adaptive mesh was allowed to refine up to a maximum level of 8. Adaptive refinement/derefinement is restricted to the region $B > 2$ G, so that the enhanced resolution is not applied to the breakout current sheet. The smallest grid cell size occurs at the inner boundary, $\Delta r = 0.33$ Mm and $R_s\Delta\theta = R_s\Delta\phi = 0.27$ Mm.

We inject shear flux to form the filament channel using the method of statistical injection of condensed helicity (STITCH; Mackay et al. 2014, 2018; Lynch et al. 2021; Dahlin et al. 2021). The injection of shear flux at the inner boundary is given by

$$\frac{\partial \mathbf{B}_\perp}{\partial t} = h^{-1}\boldsymbol{\nabla}_\perp \times (\zeta_s B_r \hat{\mathbf{r}}) \,, \tag{1}$$

where $\mathbf{B}_\perp$ is the tangential magnetic field, B_r the radial component, $\boldsymbol{\nabla}_\perp$ the tangential derivative, and h the height of the flux-injection region (one grid cell). The parameter ζ_s incorporates the local rate of rotation (i.e., vorticity) of the helicity-injecting surface flows (Antiochos 2013; Mackay et al. 2014) and reconnection of the induced twist flux at current sheets, all of which occur at sub-grid scales in this simulation. The spatial and temporal profiles of these processes are specified by

$$\zeta_s(\xi, \phi, t) = \zeta_0 f(t) \sin\left[\frac{\pi\xi}{\xi_0}\right] \sin\left[\frac{\pi\phi}{\phi_0}\right] , \tag{2}$$

where $\zeta_0 = 4.0 \times 10^{15}$ cm^2 s^{-1}, $f(t)$ is the temporal profile, $\xi = \pi/2 - \theta$ is the latitude coordinate, $\xi_0 = 0.125\pi$ (22.5°), and $\phi_0 = 0.195\pi$ (35.1°). In addition, we set $\zeta_s = 0$ where $|B| < 3.5$ G within each semi-elliptical flux region, as well as outside of the central pair of polarities that comprise the idealized active region. The instantaneous profiles for the injection of tangential flux are shown in Figure 1c,d. The flux injection is proportional to $f(t)$, which is ramped up from zero initially, held fixed at unity for an extended time, then is ramped back down to zero prior to the eruptive flare. This temporal profile is shown as the magenta curve in Figure 2 below. The magnetic field is line-tied at rest, with all velocity components fixed at zero, across the entire inner radial boundary. Otherwise, we apply the same boundary conditions used in our previous 3D ARMS eruptive-flare calculation (Dahlin et al. 2019).

4. RESULTS

Shear flux was injected gradually at the inner boundary using the STITCH method until the system erupted explosively. Through an iterative process, we identified how much injected flux was sufficient to drive the system to eruption and halted the STITCH injection just at this point. The system thereafter evolved quasi-statically, primarily due to breakout reconnection, prior to the onset of the fast dynamics. The Alfvén speed is $c_A \approx 2000$ km s^{-1} and the length scale of the active region is $L = 400$ Mm, so the characteristic Alfvén propagation time $t_A \approx 200$ s. This is significantly smaller than the time between the halting of the driving and the onset of eruption, as shown in Figure 2.

The temporal evolution of several global quantities characterizing the eruptive flare is shown in Figure 2. The energy-buildup phase extends over 0 s $< t <$ 11,500 s, whereas the eruptive-flare onset occurs at $t \approx 12,000$ s. The globally integrated magnetic free energy (solid black curve) closely follows the total shear flux in the filament channel (dashed green curve). Similar to our findings in a previous eruptive-flare study (Dahlin et al. 2019), the maximum shear field (solid green curve) rises rapidly to a maximum during the energization phase, then decreases gradually thereafter until flare onset. This behavior is due to the increase in the filament channel's cross-sectional area as the flux expands upward and outward in response to the buildup of shear magnetic pressure. Such evolution is predicted by the Aly-Sturrock limit (Aly 1984; Sturrock 1991), which argues that in both the minimum- (closed potential) and maximum- (fully open) energy states, the shear field goes to zero. Hence, the shear-field strength must peak intermediate to those energy extrema.

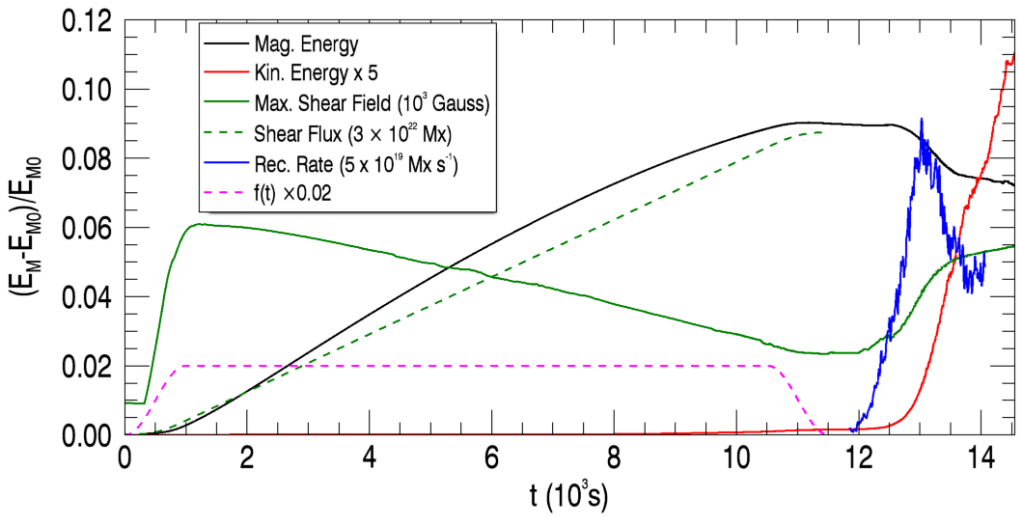

Figure 2. Global energetics during the energy buildup and the eruptive flare. The magenta curve indicates the temporal profile of shear injection, solid (dashed) green the maximum strength (total flux) of the shear field, black the magnetic free energy, red the kinetic energy, and blue the rate of reconnected flux.

The reconnection rate ($d\Phi_{rec}/dt$, where Φ_{rec} is the reconnected flux) reveals the rapid onset and fast dynamics of the eruptive flare. The rate is determined by high-cadence tracking of changes in the magnetic-field connectivity within the erupting active region (as in Dahlin et al. 2019). This process will be discussed in depth in a forthcoming study that focuses on flare-ribbon fine structure. The onset of fast reconnection precedes the rapid conversion of magnetic energy into kinetic energy, as has been noted in previous studies (Karpen et al. 2012; Dahlin et al. 2019). The maximum shear-field strength increases again at flare onset, due to the retraction and compression of flare loops that contain some shear flux. However, the majority (approximately 80%) of the filament-channel shear is ejected by the eruption. The magnetic free-energy release is much smaller because the erupting flux rope containing most of the shear remains within the simulation domain.

The formation and evolution of the filament channel are illustrated in Figure 3, which shows representative filament-channel field lines along with $\phi = 0$ cuts of B_ϕ and normalized current-density magnitude $|\mathbf{J}|\, R_s/c$. The magnetic field is initially potential (current-free), so the field lines run perpendicular to the PIL forming an unsheared arcade. As shear flux is injected into the system, the low-lying orange field lines become stretched along the ϕ direction. The red field lines are more weakly sheared, and they expand upward and sideways. The shear flux expands outward, eventually assuming an inverted teardrop shape (Fig. 3g), and a vertical current sheet forms within it. This current sheet forms only quite late in the evolution, after $t = 10,000$ s and shortly before the driving is halted. Figure 3 also shows that the region of strong shear field near the PIL is <u>not</u> identical to the region of strong shear injection; compare panels (f) and (h). The sheared field lines farther from the PIL expand more freely upward and outward, distributing the shear flux over a far greater volume than would be predicted from injection into the initial potential field. The region of strong shear that is relevant for the flare-reconnection guide field is, therefore, much narrower than the full region over which the shear is injected.

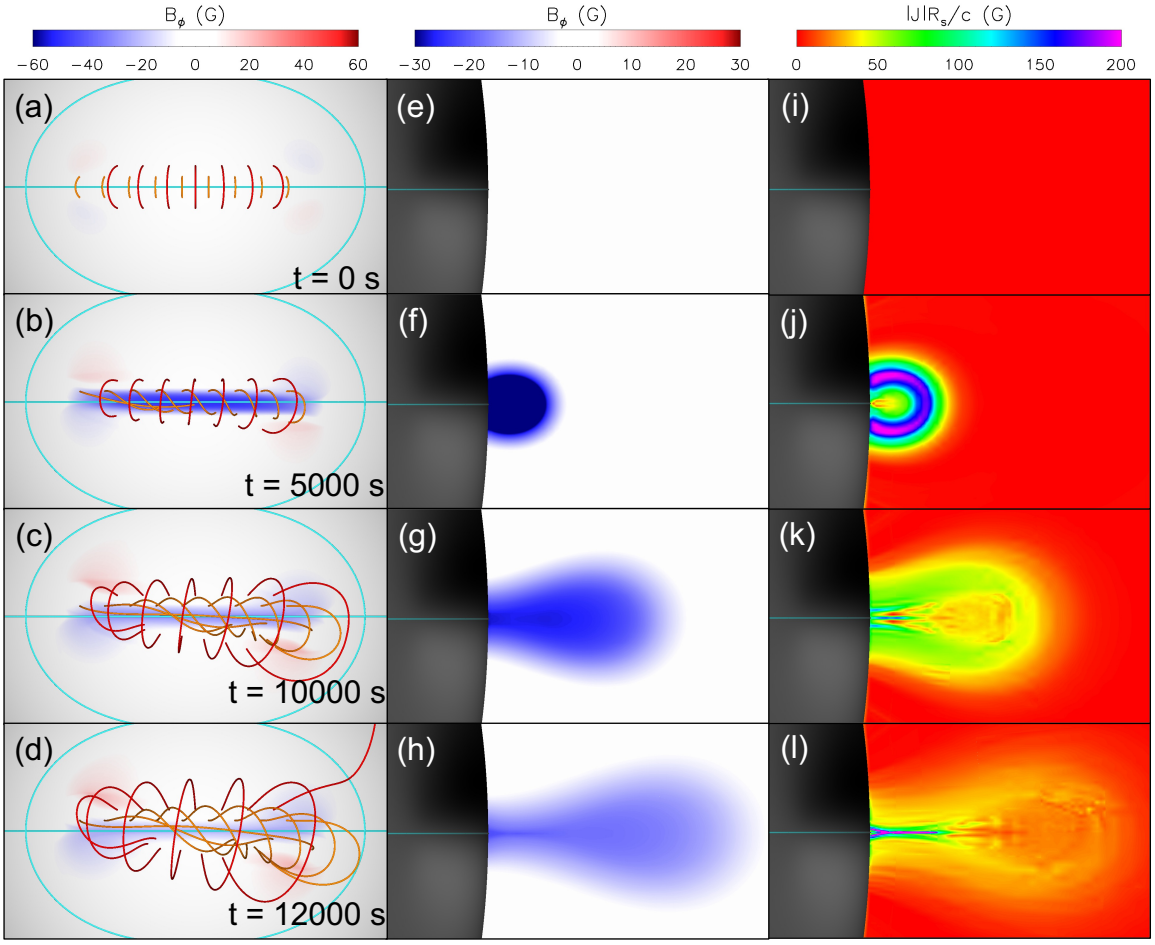

Figure 3. Energy buildup phase of the eruptive flare. (a-d) Overhead view of the filament channel, with two sets of magnetic field lines corresponding to the low-lying (orange) filament channel and overlying (red) arcade loops. Blue-to-red shading indicates B_ϕ at the inner boundary. (e-h) $\phi = 0$ cut of B_ϕ (shear/guide field). (i-l) $\phi = 0$ cut of $|\mathbf{J}|\, R_s/c$ (normalized current-density magnitude).

The flare current sheet (Fig. 3l) lengthens and its aspect ratio increases until it eventually transitions to fast reconnection. The ensuing flare reconnection is illustrated in Figure 4 by tracing field lines from a grid of 901×226 footpoints at the inner boundary over the interval 11,850 s $< t <$ 14,520 s. We identify a reconnection event as occurring at the time when the field line traced from a given footpoint shortens permanently by at least 40% relative to its maximum value. Figure 4a shows that initially the ribbons of opposite magnetic polarity are displaced in longitude and are joined by loops that are highly sheared and run nearly parallel to the PIL. As the reconnection proceeds, successively formed loops are progressively less sheared, until eventually the reconnected loops in the central region run nearly perpendicular to the PIL. This evolution is consistent with the strong-to-weak shear transition long observed in flares. We point out that the "ribbons" and "loops" discussed here are derived solely from the magnetic-field evolution and represent diagnostics of the reconnection, rather than forward modeling of the observable analogues. The latter would require a much more detailed treatment of the plasma thermodynamics and radiation. For example, the flare loops would typically be observed in EUV after a substantial time delay with respect to the corresponding Hα ribbons.

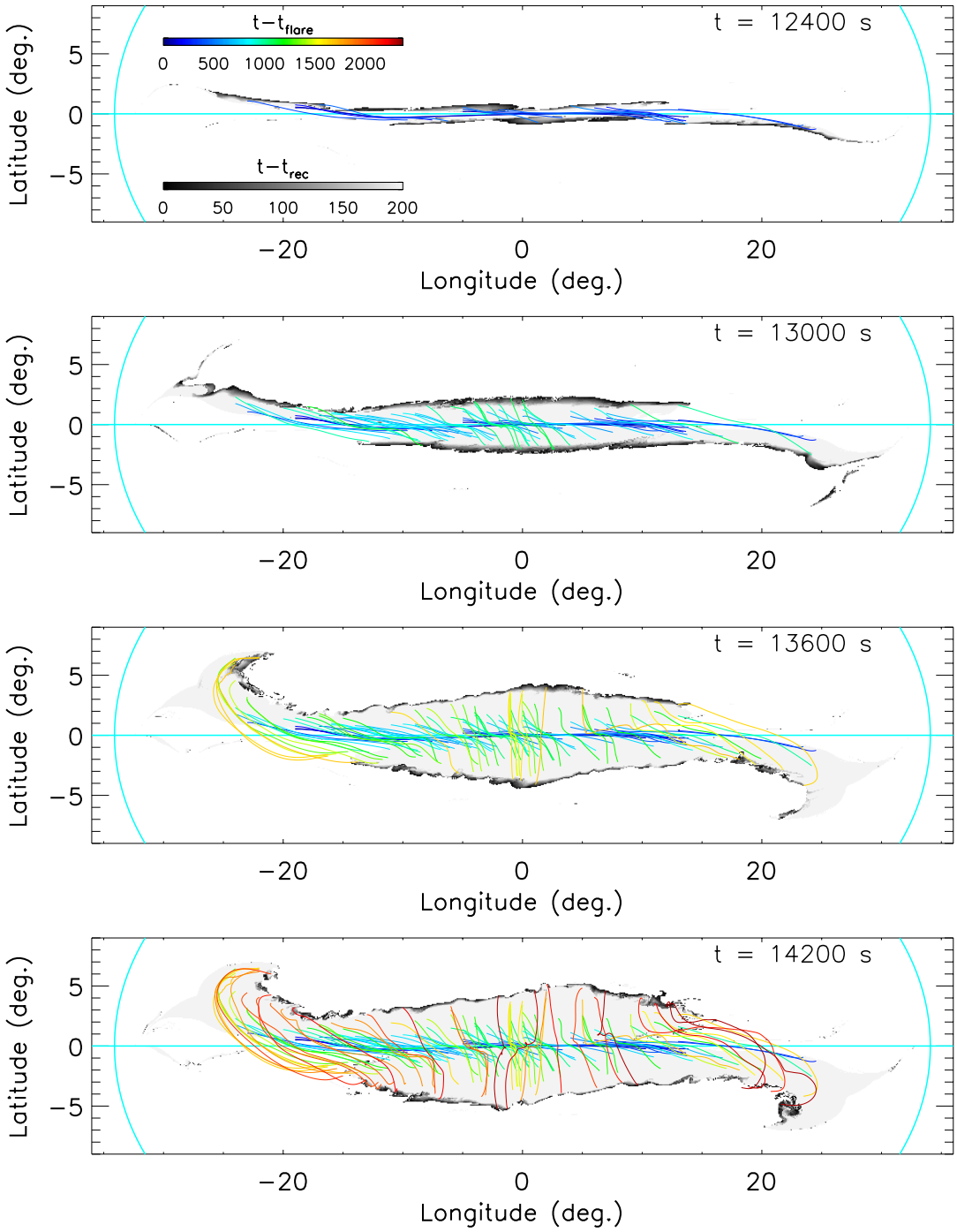

Figure 4. Flare evolution illustrated by flare ribbons and loops. Ribbons are represented by the footpoints of reconnected field lines, colored according to the time ($t - t_{\rm rec}$; gray scale) since the reconnection occurred. Flare loops are represented by reconnected field lines, colored according to the time ($t - t_{\rm flare}$; color scale) since flare onset. An animation of this figure is provided online.

In order to examine the shear evolution quantitatively, we calculate the shear angle α for all of the flare loops identified via field-line tracing (Fig. 5). The angle between the flare loop and the PIL is defined by $\alpha = \arctan(\Delta\theta/\Delta\phi)$, where the displacements of the conjugate footpoint positions are

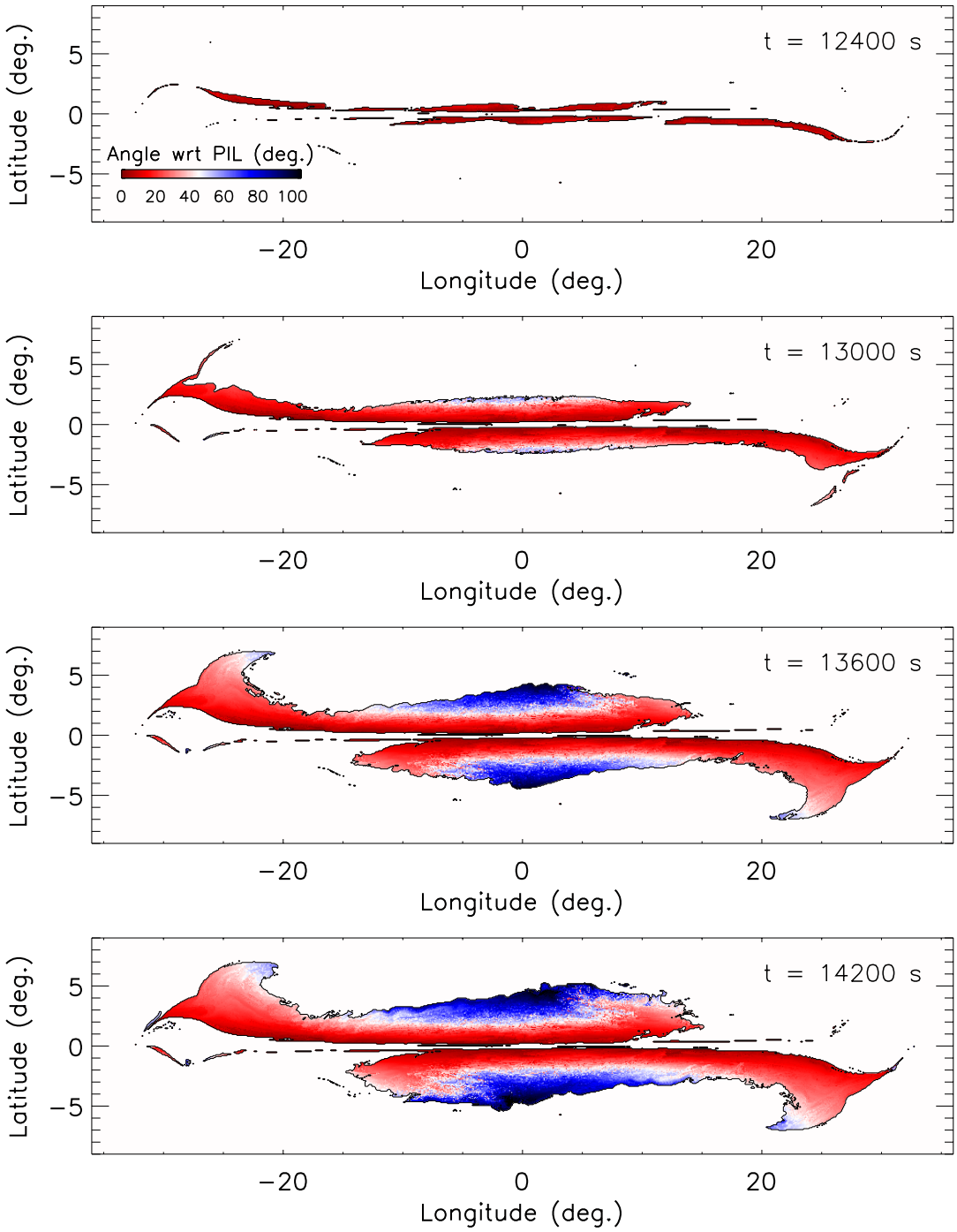

Figure 5. Cumulative flare ribbon kernel at several time steps during the evolution of the eruptive flare. Each footpoint is colorized according to the angle α that the corresponding flare loop makes with respect to the PIL, calculated according to its conjugate footpoints. An animation of this figure is provided online.

$\Delta\theta$ and $\Delta\phi$. During the initial stage of reconnection (Fig. 5a,b), all flare loops are highly sheared with respect to the PIL ($\alpha < 45°$). As reconnection proceeds (Fig. 5c,d), the decreasing shear of the central flare loops is readily apparent. However, we find a substantial variation in shear along the ribbons. Although the flare loops near the central region of the instantaneous ribbon are largely

unsheared at late times (Fig. 5c,d), the loops near the ends of the ribbons still have substantial shear. Note also that the width of the strong-shear region ($\alpha < 45°$) is much narrower than might be expected from the STITCH profile (Fig. 1c), which injects shear out to $\pm 5°$ in latitude from the PIL. We clarify the physical origins of these results in the Discussion below.

Thus far, we have focused on the evolution of the magnetic shear, which has two important characteristics: (a) an overall evolution from strong-to-weak shear, consistent with observations; and (b) substantial instantaneous variations along the flare ribbons. As previously noted, the shear in the flare loops is a clear indicator of the presence of a guide-field component at the originating reconnection site. However, quantitatively relating the measured loop shear to the upstream guide-field ratio at the flare current sheet is not simple. The guide-field parameter described in particle-acceleration simulations (e.g. Dahlin et al. 2016; Li et al. 2017; Arnold et al. 2021) refers to the upstream (relative to the reconnection site) ratio of axial/out-of-plane component to the in-plane/reconnecting component of magnetic field. In an eruptive flare model, this is challenging to calculate as the location of the current sheet evolves over time. Furthermore, in contrast to the kinetic simulations where the upstream magnetic field approaches a uniform value, there is large-scale variation in the upstream magnetic field in the eruptive-flare model. In addition, in our simulation there is the added complexity of fully 3D structure and dynamics.

We devised an algorithm to estimate the guide-field ratio, illustrated for one time step in Figure 6. First, it is necessary to identify the location of the current sheet; we examine the guide field in the center of the configuration at $\phi = 0$. At the ends of the flare current sheet (Fig. 6a), the current density bifurcates into the flare loops below and into the outgoing flux rope above. To first order, the flare current sheet can be identified as the region where the current density is single-peaked. However, the current sheet also can bifurcate internally due to transient plasmoids. Hence, we require that the current density reach its peak within a prescribed window near the equator, and we allow this window to broaden linearly in time at an empirically chosen expansion rate. The flare current sheet is taken to be the longest contiguous region that contains all of the current-density peaks within the specified window. The current density and the yellow box indicate the identified current-sheet region at $t = 12,700s$ (Fig. 6a).

To calculate the guide-field ratio, we take a constant-radius cut (dashed magenta line) through the center of the identified region. We fix the "upstream" locations as the points, approaching the current sheet from either direction, where the current density first reaches 25% of its peak value (green diamonds in Fig. 6a, dashed lines in Fig. 6b). The 25% value was chosen empirically: we found that this choice reasonably identified upstream regions throughout the entire evolution. As Figure 6b shows, the green dashed lines match well with the inflection points of both the guide-field (red) and the reconnecting-field (blue) components. At $t = 12,700$ s, the time shown in Figure 6, the guide-field ratio averaged from both sides of the current sheet is approximately unity.

We calculate the guide-field ratio in this manner over the entire interval 11,850 s $< t <$ 14,000 s. The resulting guide-field ratio is plotted in Figure 7 against the reconnection rate, $d\phi_{\rm rec}/dt$. In the convention adopted here, the ratio can be negative; we include the sign of B_ϕ in order to clarify when the guide field passes through zero. Early in the flare, the guide field is strong with magnitude exceeding unity. In this regime, the particle acceleration would be suppressed, according to recent kinetic results (Dahlin et al. 2016; Arnold et al. 2021). Thereafter, the guide field weakens to zero, even reversing its direction by the time the flare reconnection rate peaks. (This reversal occurs due

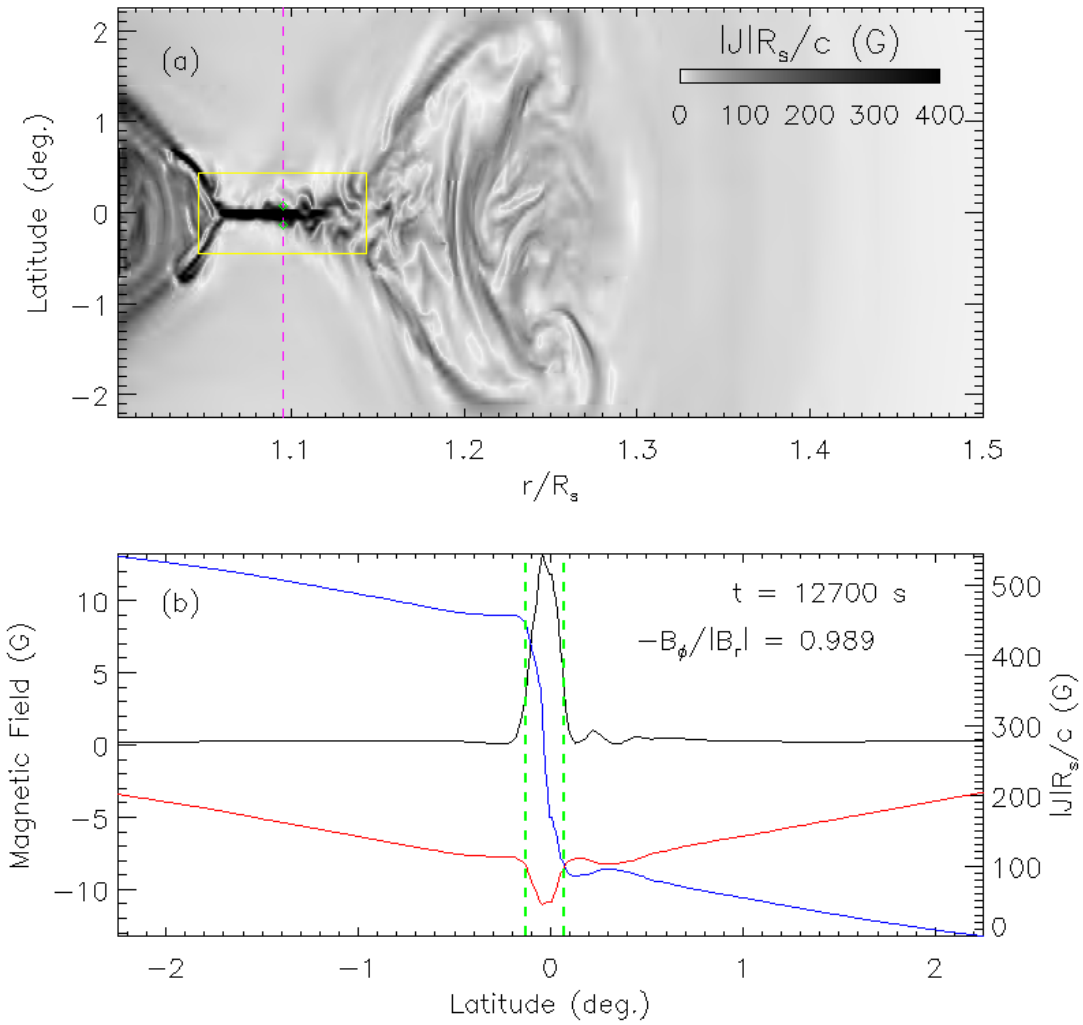

Figure 6. Illustration of method for identifying reconnection guide field. (a) Normalized current-density magnitude. The yellow box indicates the automatically identified flare current-sheet region. The dashed magenta line is a cut through the middle of the sheet. (b) Profiles of the reconnecting magnetic field component (B_r, blue), guide-field component (B_ϕ, red), and normalized current-density magnitude (black) along the cut shown in (a). Green dashed lines show where the upstream normalized guide field $-B_\phi/|B_r|$ is calculated, marked by green diamonds in (a).

to a zone of weak, reversed shear away from the PIL, evidenced by the slight opposed tilt of overlying arcade loops (red) in Fig. 3b-d.) Therefore, we conclude that the guide field (a) is large enough to suppress particle acceleration in the early phase of fast reconnection but (b) weakens rapidly to enable particle acceleration in the late phase. These two distinct phases are likely to characterize all cases of fast flare reconnection: an early, strong guide-field phase, which primarily drives heating; and a late, weak guide-field phase, which results in efficient particle acceleration.

5. DISCUSSION

The results presented in this paper demonstrate that a substantial and significantly variable guide field is an inevitable feature of flare reconnection. The guide field is represented by the shear compo-

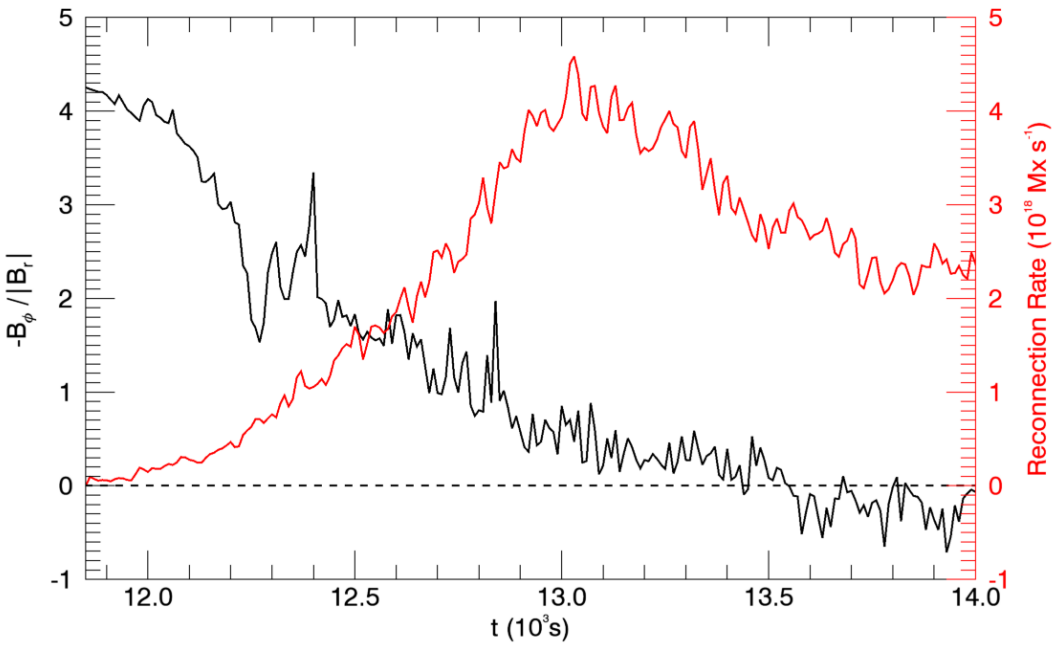

Figure 7. Guide-field ratio (black) and rate of total reconnected flux (red). During the phase of fast reconnection, the guide-field ratio weakens from ≈ 4 to ≈ 0, with a value of ≈ 0.5 at the time of peak reconnection rate.

nent of the magnetic field within the flaring filament channel, i.e., the component aligned with the polarity inversion line. Our high-resolution simulation quantifies the detailed spatial and temporal variability of the guide field throughout the flare evolution. Although the present simulation used the "breakout" mechanism (Antiochos 1998; Antiochos et al. 1999) for eruption onset, the essential features of the flare reconnection should hold for all onset mechanisms including, e.g., the torus instability (cf. Aulanier et al. 2012). This broad conclusion follows from a straightforward consideration of the generic eruptive-flare process.

The source of free energy for all CMEs/eruptive flares is the strong shear in the filament-channel magnetic field; the twist component, if any, is small by comparison prior to eruption. The eruption ejects the shear by the following process. First, a sheared filament-channel field line greatly increases its length by expanding upward and, eventually, becoming part of the CME flux rope (Fig. 3h). In a force-free field, the shear component tends to distribute itself uniformly along the field-line length (Parker 1979). Consequently, the amount of shear that remains in the flare loops, versus the amount that is ejected in the CME flux rope, is determined simply by the location of the reconnection along the loop. Early on, when the CME flux rope is first forming and the reconnection occurs near the top of the innermost field lines, most of the shear remains behind in the initially formed flare loops. As the reconnection progresses, on the other hand, the CME flux rope expands and rises rapidly, so that an increasing share of the shear is above the reconnection point and is ejected rather than being left at the Sun. The expansion of the CME flux rope is highly nonuniform in 3D, however. It is fastest and largest in the central region of the ejecta, and significantly less so in the end regions. Consequently,

the "outer" flare loops that close over the end regions retain more shear than the "inner" flare loops that close over the central region. The net result is that there is: an overall strong-to-weak shear transition in time; a highly variable shear along the instantaneous flare ribbons; and a post-eruption residual shear region that is much narrower than the initial filament channel.

Our results have two important implications for understanding flare energy release. First, recent studies demonstrate that plasmoid-driven particle acceleration is suppressed by a strong guide field (Dahlin et al. 2016; Arnold et al. 2021). In contrast, bulk plasma heating is largely insensitive to the guide field. We expect, therefore, that plasma heating should dominate over particle acceleration in the early phase of flares when the guide field is strong. This may explain so-called "hot onset" events in which strong heating is observed to precede significant particle acceleration (Hudson et al. 2021). Furthermore, strong guide fields enhance the escape of electrons from plasmoids (Dahlin et al. 2017; Dahlin 2020). This allows the particles to be accelerated repeatedly by newly forming plasmoids in adjacent regions of the flare current sheet (Dahlin et al. 2015; Dahlin et al. 2017; Li et al. 2019; Zhang et al. 2021). These processes are expected to delay further the appearance of signatures of non-thermal electrons accelerated by the flare.

Second, substantial spatial variation of the magnetic shear, in particular the persistence of strong shear near the flux-rope footpoints, implies similarly substantial variability in the guide magnetic field. The ensuing strong variations in the acceleration of energetic flare particles should manifest in the morphologies of hard X-ray footpoint and loop-top sources at the Sun, as well as the morphologies of prompt solar energetic particle events that arise from rapid escape of flare-accelerated particles into the heliosphere. In this paper, we simulated a highly idealized system with smooth large-scale structure, rather than an observed configuration with complex active-region structure at small scales. A more realistic setup could lead to even greater localization of both strong and weak guide-field regions, which could impart similar structure to the flare HXR sources. Despite these limitations, the work presented here provides a great deal of insight into understanding solar observations, through our detailed analysis of the variability of the guide magnetic field during flare reconnection.

ACKNOWLEDGMENTS

This work was supported by NASA via the SOLFER DRIVE Center at the University of Maryland, College Park, the H-ISFM program at NASA Goddard Space Flight Center, and the H-GI program at Montana State University. J.T.D. was supported by an appointment to the NASA Postdoctoral Program at NASA GSFC, administered by Universities Space Research Association under contract with NASA.

APPENDIX

The initial magnetic field configuration is given by the superposition of thirty-one magnetic dipoles placed beneath the inner boundary. The total magnetic field is given by $\mathbf{B}(\mathbf{r}) = \sum \mathbf{B}_i^{\mathrm{dip}}(\mathbf{r})$, where

$$\mathbf{B}_i^{\mathrm{dip}} = M_i \left(\frac{R_i^{\mathrm{dip}}}{|\mathbf{r} - \mathbf{r}_{0,i}} \right)^3 [3\mathbf{n_i}(\mathbf{n_i} \cdot \mathbf{m_i}) - \mathbf{m_i}],$$

$\mathbf{n}_i$ is a unit vector in the direction of $\mathbf{r} - \mathbf{r}_{0,i}$, $\mathbf{m}_i$ is the unit vector in the direction of the ith dipole moment, $R_i^{\rm dip}$ is the characteristic length scale, and M_i is the magnitude. The background solar dipole ($i = 0$) is located at $\mathbf{r}_{0,0} = [0, 0, 0]$, pointing north ($\mathbf{m}_0 = \hat{z}$) with $M_0 = 10$ G and $R_0^{\rm dip} = R_s$. The active region is comprised of two sets of dipoles oriented in the $\hat{\theta}$ direction. For $i \in [1, 21]$, $R_i^{\rm dip} = 1.5 \times 10^{10}$ cm, $M_i = 0.5$ G, and

$$\mathbf{r}_{0,i} = \left[0.928571 R_s, 0.5\pi, 0.125\pi \left(\frac{i-11}{10}\right)\right].$$

For $i \in [22, 30]$, $R_i^{\rm dip} = 3 \times 10^{10}$ cm, $M_i = 0.6$ G, and

$$\mathbf{r}_{0,i} = \left[0.928571 R_s, 0.5\pi, 0.09375\pi \left(\frac{i-26}{4}\right)\right].$$

The distribution of dipoles is adapted from (Lynch et al. 2008), to which we add a set of dipoles with larger $R_i^{\rm dip}$ to broaden the active region in latitude.

REFERENCES

Aly, J. J. 1984, ApJ, 283, 349, doi: 10.1086/162313

Antiochos, S. K. 1998, ApJL, 502, L181, doi: 10.1086/311507

—. 2013, ApJ, 772, 72, doi: 10.1088/0004-637X/772/1/72

Antiochos, S. K., DeVore, C. R., & Klimchuk, J. A. 1999, ApJ, 510, 485. http://stacks.iop.org/0004-637X/510/i=1/a=485

Arnold, H., Drake, J. F., Swisdak, M., et al. 2021, PhRvL, 126, 135101, doi: 10.1103/PhysRevLett.126.135101

Asai, A., Ishii, T. T., Kurokawa, H., Yokoyama, T., & Shimojo, M. 2003, ApJ, 586, 624, doi: 10.1086/367694

Aschwanden, M. J., & Alexander, D. 2001, SoPh, 204, 91, doi: 10.1023/A:1014257826116

Aulanier, G., Janvier, M., & Schmieder, B. 2012, A&A, 543, A110, doi: 10.1051/0004-6361/201219311

Bhattacharjee, A., Huang, Y.-M., Yang, H., & Rogers, B. 2009, PhPl, 16, 112102, doi: 10.1063/1.3264103

Bogachev, S. A., Somov, B. V., Kosugi, T., & Sakao, T. 2005, ApJ, 630, 561, doi: 10.1086/431918

Carmichael, H. 1964, A Process for Flares, Vol. 50, 451

Chen, B., Shen, C., Gary, D. E., et al. 2020, NatA, 4, 1140, doi: 10.1038/s41550-020-1147-7

Dahlin, J. T. 2020, PhPl, 27, 100601, doi: 10.1063/5.0019338

Dahlin, J. T., Antiochos, S. K., & DeVore, C. R. 2019, ApJ, 879, 96, doi: 10.3847/1538-4357/ab262a

—. 2021, ApJ, in preparation

Dahlin, J. T., Drake, J. F., & Swisdak, M. 2014, PhPl, 21, , doi: http://dx.doi.org/10.1063/1.4894484

—. 2015, PhPl, 22, doi: http://dx.doi.org/10.1063/1.4933212

Dahlin, J. T., Drake, J. F., & Swisdak, M. 2016, PhPl, 23, 120704, doi: 10.1063/1.4972082

—. 2017, PhPl, 24, 092110, doi: 10.1063/1.4986211

Demoulin, P., Henoux, J. C., Priest, E. R., & Mandrini, C. H. 1996, A&A, 308, 643

DeVore, C. R., & Antiochos, S. K. 2008, ApJ, 680, 740, doi: 10.1086/588011

Drake, J. F., Swisdak, M., Che, H., & Shay, M. A. 2006, Nature, 443, 553, doi: 10.1038/nature05116

Edmondson, J. K., & Lynch, B. J. 2017, ApJ, 849, 28, doi: 10.3847/1538-4357/aa83ba

Gaizauskas, V. 1998, in New Perspectives on Solar Prominences, ed. D. F. Webb, B. Schmieder, & D. M. Rust (San Francisco: ASP), 257–264

Gaizauskas, V., Mackay, D. H., & Harvey, K. L. 2001, ApJ, 558, 888, doi: 10.1086/322298

Gary, D. E., Fleishman, G. D., & Nita, G. M. 2013, SoPh, 288, 549, doi: 10.1007/s11207-013-0299-3

Gary, D. E., Chen, B., Dennis, B. R., et al. 2018, ApJ, 863, 83, doi: 10.3847/1538-4357/aad0ef

Gopalswamy, N., Yashiro, S., Mäkelä, P., et al. 2018, ApJL, 863, L39, doi: 10.3847/2041-8213/aad86c

Guidoni, S. E., DeVore, C. R., Karpen, J. T., & Lynch, B. J. 2016, ApJ, 820, 60, doi: 10.3847/0004-637X/820/1/60

Hirayama, T. 1974, SoPh, 34, 323, doi: 10.1007/BF00153671

Hudson, H. S., Simões, P. J. A., Fletcher, L., Hayes, L. A., & Hannah, I. G. 2021, MNRAS, 501, 1273, doi: 10.1093/mnras/staa3664

Ji, H., Wang, H., Liu, C., & Dennis, B. R. 2008, ApJ, 680, 734, doi: 10.1086/587138

Karpen, J. T., Antiochos, S. K., & DeVore, C. R. 2012, ApJ, 760, 81, doi: 10.1088/0004-637X/760/1/81

Knizhnik, K. J., Antiochos, S. K., & DeVore, C. R. 2015, ApJ, 809, 137, doi: 10.1088/0004-637X/809/2/137

—. 2017a, ApJ, 835, 85, doi: 10.3847/1538-4357/835/1/85

Knizhnik, K. J., Antiochos, S. K., DeVore, C. R., & Wyper, P. F. 2017b, ApJL, 851, L17, doi: 10.3847/2041-8213/aa9e0a

Knizhnik, K. J., Uritsky, V. M., Klimchuk, J. A., & DeVore, C. R. 2018, ApJ, 853, 82, doi: 10.3847/1538-4357/aaa0d9

Kopp, R. A., & Pneuman, G. W. 1976, SoPh, 50, 85, doi: 10.1007/BF00206193

Krucker, S., Hudson, H. S., Glesener, L., et al. 2010, ApJ, 714, 1108, doi: 10.1088/0004-637X/714/2/1108

Kumar, P., Karpen, J. T., Antiochos, S. K., Wyper, P. F., & DeVore, C. R. 2019, ApJL, 885, L15, doi: 10.3847/2041-8213/ab45f9
Kumar, P., Karpen, J. T., Antiochos, S. K., et al. 2018, ApJ, 854, 155, doi: 10.3847/1538-4357/aaab4f
Li, X., Guo, F., Li, H., & Li, G. 2015, ApJL, 811, L24. http://stacks.iop.org/2041-8205/811/i=2/a=L24
Li, X., Guo, F., Li, H., & Li, G. 2017, ApJ, 843, 21, doi: 10.3847/1538-4357/aa745e
Li, X., Guo, F., Li, H., Stanier, A., & Kilian, P. 2019, ApJ, 884, 118, doi: 10.3847/1538-4357/ab4268
Liu, W., Chen, Q., & Petrosian, V. 2013, ApJ, 767, 168, doi: 10.1088/0004-637x/767/2/168
Liu, W., Petrosian, V., Dennis, B. R., & Holman, G. D. 2009, ApJ, 693, 847, doi: 10.1088/0004-637X/693/1/847
Long, D. M., Harra, L. K., Matthews, S. A., et al. 2018, ApJ, 855, 74, doi: 10.3847/1538-4357/aaad68
Longcope, D., Unverferth, J., Klein, C., McCarthy, M., & Priest, E. 2018, ApJ, 868, 148, doi: 10.3847/1538-4357/aaeac4
Loureiro, N. F., Schekochihin, A. A., & Cowley, S. C. 2007, PhPl, 14, doi: 10.1063/1.2783986
Lynch, B. J., Antiochos, S. K., DeVore, C. R., Luhmann, J. G., & Zurbuchen, T. H. 2008, ApJ, 683, 1192. http://stacks.iop.org/0004-637X/683/i=2/a=1192
Lynch, B. J., Antiochos, S. K., Li, Y., Luhmann, J. G., & DeVore, C. R. 2009, ApJ, 697, 1918. http://stacks.iop.org/0004-637X/697/i=2/a=1918
Lynch, B. J., Masson, S., Li, Y., et al. 2016, JGRA, 121, 10, doi: 10.1002/2016JA023432
Lynch, B. J., Palmerio, E., DeVore, C. R., et al. 2021, ApJ, 914, 39, doi: 10.3847/1538-4357/abf9a9
Mackay, D. H., DeVore, C. R., & Antiochos, S. K. 2014, ApJ, 784, 164, doi: 10.1088/0004-637X/784/2/164
Mackay, D. H., DeVore, C. R., Antiochos, S. K., & Yeates, A. R. 2018, ApJ, 869, 62, doi: 10.3847/1538-4357/aaec7c
Martin, S. F. 1998, SoPh, 182, 107. https://doi.org/10.1023/A:1005026814076
Masson, S., Antiochos, S. K., & DeVore, C. R. 2013, ApJ, 771, 82, doi: 10.1088/0004-637X/771/2/82
Masson, S., Antiochos, S. K., & DeVore, C. R. 2019, ApJ, 884, 143, doi: 10.3847/1538-4357/ab4515
Masuda, S., Kosugi, T., & Hudson, H. S. 2001, SoPh, 204, 55, doi: 10.1023/A:1014230629731
Parker, E. N. 1979, Cosmical magnetic fields. Their origin and their activity
Qiu, J., Liu, W., Hill, N., & Kazachenko, M. 2010, ApJ, 725, 319, doi: 10.1088/0004-637X/725/1/319
Qiu, J., Longcope, D. W., Cassak, P. A., & Priest, E. R. 2017, ApJ, 838, 17, doi: 10.3847/1538-4357/aa6341
Sakurai, T., Shibata, K., Ichimoto, K., Tsuneta, S., & Acton, L. W. 1992, PASJ, 44, L123
Schindler, K., Hesse, M., & Birn, J. 1988, JGRA, 93, 5547, doi: 10.1029/JA093iA06p05547
Schmahl, E. J., Kundu, M. R., & Garaimov, V. I. 2006, ApJ, 643, 1271, doi: 10.1086/503151
Seaton, D. B., & Darnel, J. M. 2018, ApJL, 852, L9, doi: 10.3847/2041-8213/aaa28e
Shibata, K., & Magara, T. 2011, LRSP, 8, 6, doi: 10.12942/lrsp-2011-6
Sturrock, P. A. 1966, Nature, 211, 695, doi: 10.1038/211695a0
—. 1991, ApJ, 380, 655, doi: 10.1086/170620
Su, Y., Golub, L., & Van Ballegooijen, A. A. 2007, ApJ, 655, 606, doi: 10.1086/510065
Su, Y. N., Golub, L., van Ballegooijen, A. A., & Gros, M. 2006, SoPh, 236, 325, doi: 10.1007/s11207-006-0039-z
Temmer, M., Veronig, A. M., Vršnak, B., & Miklenic, C. 2007, ApJ, 654, 665, doi: 10.1086/509634
Veronig, A. M., Podladchikova, T., Dissauer, K., et al. 2018, ApJ, 868, 107, doi: 10.3847/1538-4357/aaeac5
Warren, H. P., Brooks, D. H., Ugarte-Urra, I., et al. 2018, ApJ, 854, 122, doi: 10.3847/1538-4357/aaa9b8
Wyper, P. F., & Pontin, D. I. 2021, arXiv e-prints, arXiv:2108.10966. https://arxiv.org/abs/2108.10966
Yang, Y.-H., Cheng, C. Z., Krucker, S., Lin, R. P., & Ip, W. H. 2009, ApJ, 693, 132, doi: 10.1088/0004-637X/693/1/132

Zhang, Q., Guo, F., Daughton, W., Li, X., & Li, H. 2021, arXiv e-prints, arXiv:2105.04521. https://arxiv.org/abs/2105.04521

Zhao, L., DeVore, C. R., Antiochos, S. K., & Zurbuchen, T. H. 2015, ApJ, 805, 61. http://stacks.iop.org/0004-637X/805/i=1/a=61